The electrical conductivity during incipient melting in the oceanic low-velocity zone

David Sifré, Emmanuel Gardès, Malcolm Massuyeau, Leila Hashim, Saswata Hier-Majumder, Fabrice Gaillard

The electrical conductivity during incipient melting in the oceanic low velocity zone.

David Sifré[1,2,3], Emmanuel Gardés[1,2,3,4], Malcolm Massuyeau[1,2,3], Leila Hashim[1,2,3], Saswata Hier-Majumder[1,2,3,5,6], Fabrice Gaillard[1,2,3].

[1]Université d'Orléans, ISTO, UMR 7327, 45071 Orléans, France.
[2]CNRS/INSU, ISTO, UMR 7327, 45071 Orléans, France.
[3]BRGM, ISTO, UMR 7327, BP 36009, 45060 Orléans, France.
[4]CEA-CNRS-ENSICAEN-Université de Caen Basse Normandie, CIMAP, UMR 6252, BP 5133, 14070 Caen, France.
[5]Department of Geology and CSCAMM, University of Maryland, MD 20742, USA.
[6]Dept. of Earth Sciences, Royal Holloway University of London Egham, Surrey, UK.

A low viscosity layer in the upper mantle, the Asthenosphere, is a requirement for plate tectonics[1]. The seismic low velocities and the high electrical conductivities of the Asthenosphere are attributed either to sub-solidus water-related defects in olivine minerals[2-4] or to a few volume percents of partial melt[5-8] but these two interpretations have shortcomings: (1) The amount of H_2O stored in olivine is not expected to be higher than 50 ppm due to partitioning with other mantle phases[9], including pargasite amphibole at moderate temperatures[10], and partial melting at high temperatures[9]; (2) elevated melt volume fractions are impeded by the too cold temperatures prevailing in the Asthenosphere and by the high melt mobility that can lead to gravitational segregation[11,12]. Here we determined the electrical conductivity of CO_2-H_2O-rich melts, typically produced at the onset of mantle melting. Electrical conductivity modestly increases with moderate amounts of H_2O and CO_2 but it dramatically increases as CO_2 content exceeds 6 wt% in the melt. Incipient melts, long-expected to prevail in the asthenosphere[10,13-15], can therefore trigger its high electrical conductivities. Considering depleted and enriched mantle abundances in H_2O and CO_2 and their effect on the petrology of incipient melting, we calculated conductivity profiles across the Asthenosphere for various plate ages. Several electrical discontinuities are predicted and match geophysical observations in a consistent petrological and geochemical framework. Below moderately aged plates (>5Ma), incipient melts most likely trigger both the seismic low velocities and the high electrical conductivities in the upper part of the asthenosphere; whereas beneath young plates[4], on top of which, seamount volcanism occurs, higher degree of melting is expected to cause high conductivities[6].

The lithosphere is a chemically depleted and mechanically strong region of the uppermost mantle, overlying the chemically enriched and mechanically weak asthenosphere [1-3,8,16]. Volatile enrichments in the asthenosphere have long been shown to trigger incipient melting[10,13-15] (that is small degree of partial melting due to small amounts of CO_2 and H_2O) in the upper part of the asthenosphere and a link between incipient melting and seismic low velocity zone has also long been suggested[13,15,17]. In this article, we demonstrate that incipient melting of the mantle by the presence of small amounts of CO_2 and H_2O can also trigger high electrical conductivities. We herein assume that the low viscosity layer, the high electrical conductivity layer (ECL) and low seismic velocity layer (LVZ) are coincident, and use the term Asthenosphere for this layer.

The Asthenosphere is characterized by high electrical conductivities[4,5,18] and reduced S-wave velocities[8,16]. While the characteristics of the Asthenosphere are commonly related to water related defects in olivine[2-4], a number of multidisciplinary observations[5-8,10,13,15,17-20] and the discovery of petit spot volcanoes[21] indicate that the Asthenosphere most likely contains partial melt.

Two issues arise when the observed features of the Asthenosphere are attributed to partial melting: (1) a few volume percentages of basaltic melt are generally required to explain high electrical conductivities, which is problematic as melt would unavoidably tend to rise if present at such high amounts[11-12] and (2) the lithosphere-asthenosphere boundary (LAB) occurs at a near constant depth of 50-75 km for both warm/young and cold/ancient lithospheres[4,5,8,16,18], where the temperature may not be sufficiently high to produce such amounts of melt.

However, incipient CO_2-H_2O rich melts, that are stable under the P-T-fO_2 conditions of the Asthenosphere[10,13-15,17,22-23], allow melting in both warm and cold regions of the Asthenosphere[17]. Low temperature carbonatite melts, composed of almost 50% CO_2, are characterized by high electrical conductivities[19], but their stability is restricted to the coldest and driest regions of the Asthenosphere[17]. Increasing temperature or water content changes the composition of the prevailing melts to intermediates between basalts and carbonatites, often described as carbonated basalts[17,22]. Very little is known about the physical properties of such intermediate volatile-rich melts (CO_2 and H_2O). In particular, their electrical properties have never been measured. In order to address the issues regarding onset of partial melting at the LAB, and to permit a test of the incipient melting model suggested by petrological studies[15,17], we performed electrical conductivity measurements on CO_2-H_2O-rich melts.

We developed a new experimental set-up, specifically adapted for liquids with high conductivities (Fig. SI1). The high performance of this modified 4-wire method, adapted to ½ inches piston cylinders, is discussed in the Methods section and figures SI2-SI5. Five melts, with CO_2 and H_2O contents ranging from 10 to 48 wt% and 0 to 10 wt%, respectively, were analysed by impedance spectroscopy in the temperature range 900 - 1500°C at a confining pressure of 3 GPa. We tested the reproducibility of the measurements by taking measurements during both cooling and heating of the samples (Fig. SI5) and we verified that decarbonation and dehydration

of samples at high temperature did not affect the conductivity results. Figure 1 reports the measured electrical conductivities as a function of reciprocal temperature. For similar water contents, the electrical conductivity of carbonated basalts is higher than that of hydrated basalts and the difference increases with an increase in the CO_2 content of the melt to a maximum of nearly one log unit. The most CO_2-rich melt has conductivities higher than 200 $S.m^{-1}$. We develop a semi-empirical law that takes into account the two parallel conductive processes operating in carbonated basalts: conduction by covalent polymer-like hydrous silicate melts and ionic conduction by carbonate melts[19].

$$\sigma_{model} = \left(\sigma_0^{H_2O} \times exp\left(\frac{-E_a^{H_2O}}{RT}\right)\right) + \left(\sigma_0^{CO_2} \times exp\left(\frac{-E_a^{CO_2}}{RT}\right)\right) \quad (1)$$

The calculated conductivities using equation 1, as shown in figure 1, reproduce our measurements and those of ref. 7 on CO_2-free hydrated basalts with an average precision of 5% in σ (see Methods). The effect of CO_2 on melt conductivity, predicted by equation 1, is negligible at low CO_2 content, but increases sharply for CO_2 content higher than 6 wt%. Such a change is most likely caused by an abrupt transition in the melt structure and properties from silicate-type to carbonate-type.

We calculate the mantle electrical conductivity for variable amounts of bulk H_2O and CO_2 contents in a partially molten peridotite. We assume that the interconnected melt is equally distributed between grain edge tubules and grain boundary melt films[18,20,24] (see Methods). The conductivity of hydrated olivine was calculated from ref. 25 and equation 1 was used for CO_2-H_2O-bearing melts. We assume that carbon is exclusively soluble in the melt[23] (carbonate units) and computed the partitioning of water between carbonated melt, pargasite, olivine, and peridotite combining ref. 9, 10 and 22. We report results for partially molten peridotite containing only H_2O (Fig. 2A) and both CO_2 and H_2O (Fig. 2B and 2C). In all simulations, partitioning constraints for CO_2 and H_2O between solids and melts impose that (1) CO_2-H_2O-rich melts can only be produced at the onset of mantle partial melting and (2) that small melt fractions always contain far more CO_2 than H_2O (see top axis in fig.2). If > 1% melting is attained, the melt volatile contents drop to values that modestly impacts on their electrical conductivity.

The CO_2-free depleted mantle, containing ca. 200 ppm H_2O[26-28], cannot be conductive at temperatures below 1350°C (i.e. $\sigma \geq 0.1$ $S.m^{-1}$), unless it contains more than ~5 vol.% basaltic melts (Fig. 2A). Only unreasonably high temperatures for the LAB (>1450°C) can make the mantle conductive with small amounts of melt (<1 vol%). Moreover, at high melt percentage, water has almost no effect on mantle conductivity, since its content in the melt remains small (i.e. <1 wt% H_2O negligibly affects basalt conductivity). If an enriched mantle is considered (500 ppm H_2O), a reasonably low melt content (1 vol.%) can trigger high conductivity but it still requires high temperature (>1325°C; Fig. SI9), and the enriched mantle is also CO_2-rich[26-28].

In presence of CO_2, the formation of incipient CO_2-rich melts (<0.5 vol.%) disproportionately increases the effective electrical conductivity of the mantle (Fig. 2B and 2C). For example, in the depleted mantle, containing 200 ppm H_2O and 200 ppm CO_2[26] and fuelling the dominant part of MORBs[27-28], 0.1-0.15 vol.% of melt at 1325°C can explain the high electrical conductivity of the ECL reported in oceanic domains[5,18,29]. The melt is a carbonated basalt, typically containing 15-35 wt% CO_2 and about 2-3 wt% H_2O (Fig.2B). Remarkably, the enriched mantle[27-28] with 500 ppm H_2O and 500 ppm CO_2 can produce high conductivities at temperature and melt fractions as low as 1050°C and 0.2 vol%. We also notice that incipient melting of the enriched mantle triggers conductivities that are 2.5 times greater than the depleted mantle making variations in electrical conductivity a powerful probe of the chemical enrichment in the upper mantle.

The stability of incipient melts in the upper part of the asthenosphere has long been shown by petrological constraints[13-15], that are not considered in Fig. 2. The P-T region of incipient melting in peridotite is shown in Fig. SI8 together with the stability domain of pargasite, that is the main solid host for water in peridotite containing more than 150-200 ppm[10]. We calculate that the presence of pargasite restricts the amount of water to 40-50 ppm in olivine, according to partition coefficient among peridotite minerals[9,10]. Pargasite is however unstable at T>1070°C[10] and its occurrence must be merely considered for the enriched mantle (>200 ppm H_2O). Based on the P-T phase diagram of Fig. SI8 and considering oceanic geotherms at 23.5, 35 and 70 Ma, we have calculated 1D conductivity profiles illustrating the impact of several petrological discontinuities (Fig. 3). We have considered the depleted mantle (200 ppm H_2O plus CO_2 varying from 100 to 500 ppm) and the enriched mantle (500 ppm H_2O and 500 ppm CO_2). Variable CO_2 contents in the depleted mantle account for the fact that MORBs have degassed their CO_2 and the carbon content of their source is therefore highly uncertain[26-28].

The upper discontinuity (Fig. 3) predicted by our model is the beginning of incipient melting at ~50 km depth for young/warm plates and at ~70 km for colder/older plates. This discontinuity marks the thermodynamic boundary between CO_2-rich melt and CO_2-rich vapour[14]: the melt being stable at greater depth. In the case of an enriched mantle, an additional discontinuity occurs due to the pargasite dehydration melting reaction (producing CO_2-H_2O rich, low SiO_2 melt) that can be shallower than the previously described discontinuity for young plates (ie. 23.5Ma) and deeper for old plates (70 Ma). At 35 Ma, these two discontinuities occur at the same depth (60 km). The lowest discontinuity shown in Fig. 3 occurs in the depth interval 120-150 km and is described as the region of redox melting[22,23]; that is the boundary separating diamonds from CO_2-rich melts, the melt being stable at shallower depth. Incipient melting, which triggers the conductive region of the asthenosphere, is therefore permitted between the redox melting lower boundary and the decarbonation upper boundary and this agrees well with electromagnetic observations in oceanic domains[4,5,18,22,29], though ref. (29) indicates slightly deeper ranges.

The increase in conductivity in the incipient melting region is major, being half a log-unit for the depleted mantle (200 ppm CO_2) and more than one log-unit for the mantle containing 500 ppm CO_2. High conductivities of 0.1 S/m or more can be reached for CO_2 contents as low as 300 ppm

in the case of young plates. Note that the surprising effect of water (Fig. 3), where incipient melting in a mantle with 500 ppm H_2O and 500 ppm CO_2 induces lower conductivities than in a mantle with 200 ppm H_2O the same amount of CO_2. The imaging of the 23.5 Ma old LAB by ref. 5 at ~50 km depth revealed conductivities of 0.1-0.2 $S.m^{-1}$. These are definitely not explainable by melting of a CO_2-free H_2O-depleted mantle, since too high temperatures and/or too high melt contents are demanded (Fig. 2). They cannot be explained by pargasite dehydration melting in a CO_2-free H_2O-enriched mantle either, as this process cannot produce high enough conductivities (Fig. 3, Fig. SI9). Once deciphered in a petrological framework, the conductivities of the LAB in ref. 5 can be reached by incipient melting of a mantle containing 400 ppm CO_2 (Fig. 3). We recall that ref. 5 introduced moderate electrical anisotropy in the inversion of their magnetotelluric data whereas we merely discuss here the geometric mean conductivity, which is much less model dependent.

The presence of CO_2-rich melts in the asthenosphere not only better explains the electrical properties of the Asthenosphere, but also explains the weak dependence of the lithosphere thickness on the age of the oceanic crust (Fig. 4). The bottom of the lithosphere in Fig. 4 marks a seismic discontinuity characterised by a reduction in S-waves velocity of 5 to 15 %[8,16]. This discontinuity cannot be caused by partial melting of a dry or water under-saturated mantle, as this may only occur at higher depths and temperatures[9] (see blue melting curve on Fig. 4). Previously suggested melting reactions such as the dehydration melting of amphibole[10] also fail to reproduce the depth-age relationships of the LAB (Fig. 4). Remarkably, the CO_2+H_2O melting curve[14], which delimits the upper boundary of the incipient melting region already shown in Fig. 3, ranges from 50 km down to 80 km depths from the youngest to the oldest lithospheres (purple curve in Fig. 4). This correlates pretty well with the bottom of the lithosphere as imaged by the seismic discontinuity. The lower limit of incipient melting, i.e. the redox melting[22,23], matches also well the lower part of the seismic low velocity zone[8] at depth of about 140-180 km. At low pressures, above the incipient melting region, the decarbonation of the melt forms an impermeable layer in which buoyant CO_2-rich melts are frozen into clinopyroxene-rich residue (with pargasite) and CO_2-rich fluids (Fig.4). Melting is therefore permitted in the Asthenosphere and the melt cannot rise through the LAB because of the existence of this melt-freezing boundary (see Methods). It is only where the mantle is hot enough to suppress the freezing reaction (that is melting does not anymore require CO_2) and where melt fractions are large enough[12] (2-5 vol%) that melts can rise to the LAB. This occurs for young plates (<5Ma), where volcanic seamounts are observed, and this has also been related[6] to the electrical properties of the young LAB[4].

Incipient melting has long been described as a key petrological process operating in the seismic low velocity region marking the upper asthenosphere[13,15,17]. The mantle geochemistry and petrology in this region argues for production of incipient CO_2-enriched melts[9,10,13,15]. We demonstrate that these melts have conductivities of hundreds of S/m, much higher than CO_2-free hydrated melts or hydrated minerals. Our modelling, despite unavoidable simplifications, considers geochemical and petrological constraints and indicates that mantle with small fractions

of CO_2-rich melts at 50-150 km reproduces the electrical properties as well as the depth of the LAB pretty well, whereas CO_2-free systems yields too poor or no agreement with geophysical observations. The presence of CO_2-rich incipient melts in the Asthenosphere has important implications for radiogenic heat production as such melts are enriched in heat-producing elements like K-U-Th[30]. Moreover, the involvement of CO_2-rich incipient melts is also recognized in petrological processes occurring in the continental and in the cratonic LAB[30]. The Asthenosphere - incipient melting association we suggest here can therefore be extended to geodynamic settings other than the oceanic domains. It remains however to be defined how the mechanical strength of the Asthenosphere can be impacted by small amount of CO_2-H_2O-rich melts and how this can be connected to plate motions.

METHODS SUMMARY

Starting materials were mixtures of basaltic glass and hydrated Ca-Mg-Carbonates, so that water and CO_2 were all together introduced in our sample with a constant molar CO_2/H_2O ratio of 2 (in mole; see Table SI1). Two dry carbonate melts were also investigated. The extent of dehydration and decarbonation of our samples during high temperature-high pressure experiments were shown to be small (Table SI1 vs. SI2). The effect of H_2O was disentangled from that of CO_2 by using published experimental conductivity measurements on hydrated basalts[7] and the empirical equation 1. This empirical simplification is in line with the effect of water on the conductivity of carbonated melts that we determined here (circles vs. squares in Fig. SI5): it is moderate and almost similar to that recently determined for basalts[7]. Equation 1 was used for simulations in Fig. 2 and Fig. 3 remaining within the range of experimentally investigated H_2O and CO_2 contents.

Figures 2 and 3 have been constructed considering that incipient melts are well connected[20,24]. Ref. 24 constitutes the only work specifically tackling the connectivity of incipient carbonated melts in olivine and it shows interconnection at the small melt fractions we are considering. Ref. 20 confirmed the good connection for melt contents of ~1%. Mixtures of melt tubes and melt films have been considered in our plots; the difference between both geometries implies conductivities differing by ca. 0.2 log-units.

The isotherms in figure 4 were obtained considering the sudden half space cooling model with similar parameters as in ref. 8. The use of more complicated models such as the plate model (see ref. 17, which is, conversely to us, *a priori* deciding for a thickness of the lithosphere) yields similar isotherms[8] for the moderate depths we discuss here.

REFERENCES

1. Höink, T., Jellinek, A.M. & Lenardic, A. Viscous coupling at the lithosphere-asthenosphere boundary.*Geochem.Geophys. Geosyst.* **12**, Q0AK02 (2011).

2. Hirth, G. & Kohlstedt, D.L. Water in the oceanic upper mantle: Implications for rheology, melt extraction and the evolution of the lithosphere. *Earth Planet. Sci. Lett.* **144**, 93-108 (1996).

3. Karato, S. On the origin of the asthenosphere. *Earth Planet. Sci. Lett.* **321**, 95-103 (2012).

4. Evans, R.L., Hirth, G., Baba, K., Forsyth, D., Chave, A. & Mackie, R. Geophysical evidence from the MELT area for compositional controls on oceanic plates. *Nature* **437**, 249-252 (2005).

5. Naif, S., Key, K., Constable, S. & Evans, R.L. Melt-rich channel observed at the lithosphere-asthenosphere boundary, *Nature* **495**, 356-359 (2013).

6. Caricchi, L., Gaillard, F., Mecklenburgh, J. & Le Trong E. Experimental determination of electrical conductivity during deformation of melt-bearing olivine aggregates: Implications for electrical anisotropy in the oceanic low velocity zone. *Earth Planet. Sci. Lett.* **302**, 81-94 (2011).

7. Ni, H., Keppler, H. & Behrens, H. Electrical conductivity of hydrous basaltic melts: implications for partial melting in the upper mantle. *Contrib. Mineral. Petrol.* **162**, 637–650 (2011).

8. Schmerr, N. The Gutenberg discontinuity: melt at the lithosphere-asthenosphere boundary. *Science* **335**, 1480-1483 (2012).

9. Hirschmann, M., Tenner, T., Aubaud, C. & Withers, A.C. Dehydration melting of nominally anhydrous mantle: The primacy of partitioning. *Phys. Earth Planet. Inter.* **176**, 54-68 (2009).

10. Green, D.H., Hibberson, W.O., Kovács, I. & Rosenthal, A. Water and its influence on the lithosphere-asthenosphere boundary. *Nature* **467**, 448-U97 (2010).

11. Hier-majumder, S., Courtier, A. Seismic signature of small melt fraction atop the transition zone. *Earth Planet. Sci. Lett.* **308**, 334–342 (2011). doi:10.1016/j.epsl.2011.05.055.

12. Faul, U. H., Melt retention and segregation beneath mid-ocean ridges. *Nature* **410**, 920–3 (2001). doi:10.1038/35073556.

13. Presnall, D.C. & Gudfinnsson, G.H. Carbonate-rich melts in the oceanic low-velocity zone and deep mantle. *Geol. Society of America*, Special Papers **388**, 207-216 (2005).

14. Wallace, M.E. & Green, D.H. An experimental determination of primary carbonatite magma composition. *Nature* **335**, 343-346 (1988)

15. Green, D.H., Liebermann, R.C, Phase-equilibra and elastic properties of a pyrolite model for oceanic upper mantle, Tectonophysics **32**, 61-92 (1976)

16. Fischer, K.M., Ford, H.A., Abt, D.L. & Rychert, C.A. The Lithosphere-Asthenosphere Boundary. *Annual Review of Earth and Planetary Sciences* **38**, 551-575 (2010).

17. Hirschmann, M.M. Partial melt in the oceanic low velocity zone. *Phys. Earth Planet. Inter.* **179**, 60–71 (2010).

18. Utada, H., Baba, K., Estimating the electrical conductivity of the melt phase of a partially molten asthenosphere from seafloor magnetotelluric sounding data, *Physics of the Earth and Planetary Interiors* (2013), doi: http://dx.doi.org/10.1016/j.pepi.2013.12.004.

19. Gaillard, F., Malki, M., Iacono-Marziano, G., Pichavant, M. & Scaillet, B. Carbonatite melts and electrical conductivity in the asthenosphere. *Science* **322**, 1363-1365 (2008).

20. Yoshino, T., Laumonier, M., McIsaac, E. & Katsura, T. Electrical conductivity of basaltic and carbonatite melt-bearing peridotites at high pressures: Implications for melt distribution and melt fraction in the upper mantle. *Earth Planet. Sci. Lett.* **295**, 593–602. (2010).

21. Hirano, N., Takahashi, E., Yamamoto, J. et al. Volcanism in Response to Plate Flexure. *Science* **313**, 1426-1428 (2006).

22. Dasgupta, R., Mallik, A., Tsuno, K., Withers, A.C., Hirth, G. & Hirschmann, M.M. Carbon-dioxide-rich silicate melt in the Earth's upper mantle. *Nature* **493**, 211-U222 (2013).

23. Stagno, V., Ojwang, D.O., McCammon, C.A. & Frost, D.J. The oxidation state of the mantle and the extraction of carbon from Earth's interior. *Nature* **493**, 84 (2013).

24. Minarik, W.G. & Watson, E.B. Interconnectivity of carbonate melt at low melt fraction. *Earth Planet. Sci. Lett.* **133**, 423-437 (1995).

25. Jones, A. G., Fullea, J., Evans, R. L., Muller, M.R. Water in cratonic lithosphere: Calibrating laboratory determined models of electrical conductivity of mantle minerals using geophysical and petrological observations. *Geochem. Geophys. Geosyst.* **13**, Q06010 (2012)

26. Cartigny, P., Pineau, F., Aubaud, C. & Javoy, M. Towards a consistent mantle carbon flux estimate: Insights from volatile systematics (H2O/Ce, δD, CO2/Nb) in the North Atlantic mantle (14° N and 34° N). *Earth Planet. Sci. Lett.* **265**, 672–685 (2008).

27. Marty B., The origins and concentrations of water, carbon, nitrogen and noble gases on Earth. *Earth Planet. Sci. Lett.* **313-314**, 56–66 (2012).

28. Dasgupta, R., Hirschmann, M.M., The deep carbon cycle and melting in Earth's interior. *Earth Planet. Sci. Lett.* **298**, 1–13 (2010)

29. Lizarralde, D., Chave, A., Hirth, G., Schultz, A., Northeastern Pacific mantle conductivity profile from long-period magnetotelluric sounding using Hawaii-to-California submarine cable data. *J. Geophys. Res.*, **100(B9)**, 17837–17854 (1995).

30. O'Reilly, S.Y. & Griffin, W.L. The continental lithosphere-asthenosphere boundary: Can we sample it? *Lithos* **120**, 1-13 (2010).

Supplementary information (9 figures, 5 Tables)

Acknowledgments- This work, part of the ElectroLith project, benefited from funding by the European Research Council (ERC project #279790) and the French agency for research (ANR project # 2010 BLAN62101). SH-M acknowledges support from the NSF grant EAR1215800 and a grant from the University of Orléans.

Authors contributions- F.G. is leading the project and wrote the first draft. All authors equally contributed to the writing. D.S. and F.G. developed the experimental setup and D.S. performed the conductivity measurements. S.H-M contributed to the discussion and provided editorial assistance with manuscript. D.S. and L.H. did figure 1, E.G. and L.H. did figure 2, D.S. did figure 3 and L.H., M.M. did figure 4.

METHODS:

Starting materials

Electrical measurements were performed on five mixtures: 2 dry carbonated melts (CO_2=44 - 48wt%), a hydrous carbonated melt (CO_2 =25.9 wt%; H_2O=10.2 wt%) and 3 hydrous carbonated basalts (CO_2 = 10.39 to 23.32 wt%; H_2O=4.43 to 9.22 wt.%, Table SI1). Starting materials used to obtain these mixtures were natural dolomite ($MgCa(CO_3)_2$), a natural basalt (popping rock[31]), salt (NaCl), sodium carbonates (Na_2CO_3) and brucite ($Mg(OH)_2$) (Table SI1).

Experiments

All experiments were performed at 3 GPa in ½-inches piston cylinders (graphite-Pyrex-talc assemblages), which was connected to a 1260 Solartron Impedance/Gain Phase Analyzer for electrical conductivity measurements. The temperature was measured with a B-type thermocouple localized on sample top (Fig. SI1). Oxygen fugacity (fO_2) was not controlled during the measurements but the presence of graphite (furnace) and molten carbonates (sample) should imply an oxygen fugacity close to FMQ-2[23].

We have developed a new protocol specifically adapted for electrical conductivity measurements on highly conductive and molten materials (Fig. SI1). The new design employs a pseudo-4-wire configuration, which removes the electrical contribution of the electrical cell itself (Fig. SI2). Such a configuration previously adapted at 1 atm[19,32] is here shown necessary for measurements on H_2O-CO_2-rich melts at 3 GPa.

Cold pressed pellets (5 mm outer diameter) were cored in their centre in order to place an inner Pt electrode (1 mm). A Pt foil surrounding the cylindrical sample was used as outer electrode. An alumina jacket isolated the entire electrical cell from the graphite furnace. The sample impedance was measured between the two electrodes arranged in a co-axial geometry[33,34]. The inner electrode was connected to the impedance spectrometer via the two wires of the thermocouple[34]. The outer electrode was connected to a nickel cylinder (located 5 mm above the sample) that was mounted in series with two additional wires (B-type thermocouples) (Fig. SI1).

Data reductions and uncertainties

The electrical conductivities of the samples were calculated from the measured resistances using the following relationship[33,34]:

$$\sigma = \frac{\ln(r_{out}/r_{in})}{2\pi hR} \quad (2)$$

with σ being the electrical conductivity in S.m^{-1}, r_{out}, r_{in}, h, respectively the outer radius, the inner radius and the height of the samples in m, and R, the resistance of the sample in Ω (Fig. SI3 and SI4).

Uncertainties in σ were calculated as a function of geometrical factors of the samples (Fig. SI4) and propagating errors of each measured resistance. The uncertainties on σ are 7 % on average for all measurements and reach a maximum of 16% on HCB-4.

Sample characterization

Scanning electron microscope (SEM) imaging and electron microprobe analyses (EMPA) were systematically operated after each experiment. Determination of r_{out}, r_{in} and h by SEM imaging showed an average decrease of 20% compared to the initial geometry, most likely due to porosity loss during melting (Fig. SI4). No melt leak was observed and the entire sample remained sandwiched between the MgO plugs and the electrodes.

EMP analyses were conducted at 15 KeV, 10 nA and 10 sec counting on peak elements. The beam size (100 μm x 100 μm) was adapted to obtain average chemical compositions, smoothing the heterogeneities due to quench crystallizations. Comparison of compositions before and after experiments shows no contamination by the MgO surrounding the sample and no considerable volatile loss from the sample to the surrounding assemblages (Tables SI1, SI2). CO_2 content were determined using the by-difference method[22] and indicate negligible decarbonation.

An elemental analyser, type Flash 2000 (Thermo Scientific; see SI), was used to measure H_2O content of sample (before and) after experiments. Samples are heated to >1500°C and the released H_2O is reduced into elemental H being finally detected by a highly sensitive thermal conductivity detector. This gives water content with a precision of +/- 0.5 wt%. We observed a negligible dehydration during conductivity measurements.

Conductivity Results and Modelling

Figure SI5 shows the good reproducibility of the electrical measurements during heating and cooling cycles. The conductivity-temperature relationships for each sample were fitted using an Arrhenius law and the calculated pre-exponential factors and activation energies are presented in Table SI4.

In the semi-empirical law (equation 1), the pre-exponential factor σ_0 and the activation energy E_a for both H_2O and CO_2 terms are related by a compensation law[35,36] (Fig. SI5)

$$ln\sigma_0^{volatile} = \left(E_A^{volatile} \times d\right) + e \quad (3)$$

the decrease of activation energy as a function of volatile content is exponential

$$E_A^{volatile} = a \times exp\left(-b \times C^{volatile}\right) + c \quad (4)$$

$C^{volatile}$ is the CO_2 and H_2O content in wt%. The optimized parameters a, b, c, d and e are given in Table SI5 together with their propagated uncertainties. Our model reproduces the experimental measurements on σ within an average error of 5% (maximum 10%).

Figures 2 & 3

The bulk rock is considered as a peridotite containing a fraction of interconnected melt, where volatiles partition between the solid and the melt phase. The bulk H_2O content is related to H_2O in melt and in peridotite as:

$$C_{H_2O}^{melt} = \frac{C_{H_2O}^{bulk}}{X_m^{melt}+(1-X_m^{melt})D_{H_2O}^{perid/melt}} \text{ and } C_{H_2O}^{perid} = \frac{C_{H_2O}^{bulk} D_{H_2O}^{perid/melt}}{X_m^{melt}+(1-X_m^{melt})D_{H_2O}^{perid/melt}} \quad (5)$$

where X_m^{melt} is the mass fraction of melt and $D_{H_2O}^{perid/melt}$ is the partition coefficient of H_2O between peridotite and melt (0.007, i.e. average partition coefficient over 1.5-4 GPa[9,37]).

We assume that CO_2 distributes exclusively in the liquid phase[23,38], i.e. $D_{CO_2}^{perid/melt} = 0$.

Conversion from mass to volume fraction of melt is done considering volume properties of silicate melts[39] and carbonate melts[40,41]. The conductivity of the melt $\sigma_{melt}(C_{H_2O}^{melt}, C_{CO_2}^{melt}, T)$ was calculated using equation 1. The conductivity of the peridotite was assumed to be controlled by that of hydrous olivine[25].

The bulk conductivity was calculated using the mean of tube[42-44] and film[44-47] geometries resulting in values almost similar to refs (20, 46).

Melt fraction in Fig. 3 was approximated as[48] $X_m^{melt} = 2.5\times CO_2^{bulk} + 6\times H_2O^{bulk}$.

Buoyant basalts versus incipient melts

An impermeable layer has been suggested to limit or prevent the melt prevailing in the LAB from rising to the surface[49]. The rate of melt ascent due to buoyancy is otherwise expected to be of the order of several cm/year[11,12], if melt content is 3-5 vol. %. Our model of incipient melting implies an impermeable boundary that is caused by phase relationships[14], i.e. a thermodynamic boundary through which melt cannot rise. We furthermore emphasise the limited melt mobility[50] at the small melt fraction of interest as, in particular, surface tensions would unavoidably tend to retain the buoyant melt[51]. To conclude, if basalts, being anyway not thermodynamically stable in the asthenosphere, tend to migrate out of the asthenosphere[52], small melt fractions may in contrast be mechanically stable in the LAB.

ADDITIONAL REFERENCES FOR METHODS:

31. Javoy, M. & Pineau, F. The volatiles record of a "popping" rock from the Mid-Atlantic Ridge at 14 ° N: chemical and isotopic composition of gas trapped in the vesicles. *Earth Planet. Sci. Lett.* **107**, 598-611 (1991).

32. Pommier, A., Gaillard, F., Malki, M. & Pichavant, M. Methodological re-evaluation of the electrical conductivity of silicate melts. *Am. Mineral.* **95**, 284-291 (2010).

33. Gaillard, F. Laboratory measurements of electrical conductivity of hydrous and dry silicic melts under pressure. *Earth Planet. Sci. Lett.* **218**, 215-228 (2004).

34. Hashim, L., Gaillard, F., Champallier, R., Le Breton, N., Arbaret, L., Scaillet, B. Experimental assessment of the relationships between electrical resistivity, crustal melting and strain localization beneath the Himalayan-Tibetan belt. *Earth Planet. Sci. Lett.* **373**, 20-30 (2013) doi:10.1016/j.epsl.2013.04.026.

35. Pommier, A., Gaillard, F., Pichavant, M. & Scaillet, B. Laboratory measurements of electrical conductivities of hydrous and dry Mount Vesuvius melts under pressure. *J. Geophys. Res. Solid Earth* **113**, B05205 (2008).

36. Tyburczy, J. & Waff, H.S. Electrical conductivity of molten basalt and andesite to 25 kilobars pressure: Geophysical significance and implications for the charge transport and melt structure. *J. Geophys. Res.* **88**, 2413-2430 (1983).

37. Katz, R. F., M. Spiegelman, and C. H. Langmuir, A new parameterization of hydrous mantle melting, Geochem. Geophys. Geosyst., 4(9), 1073, doi:10.1029/2002GC000433, 2003.

38. Keppler, H., Wiedenbeck, M. & Shcheka, S.S. Carbon solubility in olivine and the mode of carbon storage in the Earth's mantle. *Nature* **424**, 414-416 (2003).

39. Lange, R.A. & Carmichael, I.S.E. Thermodynamic properties of silicate liquids with emphasis on density thermal expansion and compressibility. *Rev. Mineral*. **24**, 25-64 (1990).

40. Liu, Q. & Lange, R.A. New density measurements on carbonate liquids and the partial molar volume of the CaCO3 component. *Contrib. Mineral. Petrol.* **146**, 370-381 (2003).

41. Guilllot B. & Sator N. Carbon dioxide in silicate melts: A molecular dynamics simulation study. *Geoch. Cosmoch. Acta* **75**, 1829–1857 (2011).

42. ten Grotenhuis, S. M., Drury, M. R. Spiers, C. J. & Peach, C. J. Melt distribution in olivine rocks based on electrical conductivity measurements, *J. Geophys. Res.* **110**, B12201 (2005).

43. Hammouda, T., Laporte, D. Ultrafast mantle impregnation by carbonatite melts. *Geology* 28, 283–285 (2000).

44. Glover, P.W.J., Hole, M.J. & Pous J. A modified Archie's law for two-conducting phases. *Earth Planet. Sci. Lett.* **180**, 369-383(2000).

45. Partzsch, G.M., Schilling, F.R. & Arndt, J. The influence of partial melting on the electrical behaviour of crustal rocks: laboratory examinations, model calculations and geological interpretations. *Tectonophysics* **317**, 189-203 (2000).

46. Yoshino, T., McIsaac, E., Laumonier, M. & Katsura, T. Electrical conductivity of partial molten carbonate peridotite. *Phys. Earth Planet. Inter.* **194**, 1-9 (2012).

47. Garapić, G., Faul, U.H., Brisson, E. High-resolution imaging of the melt distribution in partially molten upper mantle rocks: evidence for wetted two-grain boundaries. *Geochem. Geophys. Geosyst.* **14**, 556–566 (2013).

48. Green, D.H., Falloon, T.J. Primary magmas at mid-ocean ridges, "hotspots," and other intraplate settings: Constraints on mantle potential temperature. *Geol. Society of America*, Special Papers **388**, 217-247 (2005) 10.1130/0-8137-2388-4.217.

49. Katz, R.F., Weatherley, S.M. Consequences of mantle heterogeneity for melt extraction at mid-ocean ridges. *Earth Planet. Sci. Lett.* **335-336**, 226-237 (2012).

50. Hier-Majumder, S., Ricard, Y. & Bercovici, D. Role of grain boundaries in magma migration and storage. *Earth Planet. Sci. Lett.* **248**, 735-749 (2006).

51. Takei, Y.& Holtzman, B. K. Viscous constitutive relations of solid-liquid composites in terms of grain boundary contiguity: 1. Grain boundary diffusion control model. *J. Geophys. Res.* **114**, B06205 (2009) http://dx.doi.org/10.1029/2008JB005850.

52. Sakamaki, T., Suzuki, A., Ohtani, E., Terasaki, H., Urakawa, S., Katayama, Y, Funakoshi, K-I, Wang, Y., Hernlund, J.W., Ballmer, M.D. Ponded melt at the boundary between the lithosphere and asthenosphere. *Nature Geosciences* **6**, 1041–1044 (2013) doi:10.1038/ngeo1982.

FIGURES CAPTIONS:

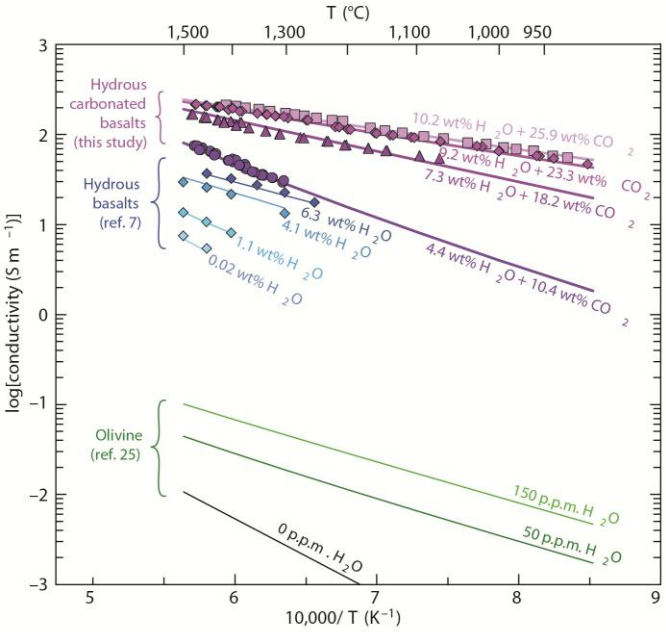

Figure 1. Electrical conductivity of hydrous carbonated basalts vs. hydrated basalts and hydrous olivine. The conductivities of the hydrous carbonated basalts experimentally measured in this study are by far the highest, reaching up to 200 S/m and being about one and four order of magnitude higher than hydrated basalts[7] and hydrous olivine[25], respectively. The fitting curves are calculated according to our conductivity model for CO_2- and H_2O-bearing melts (Eq. 1).

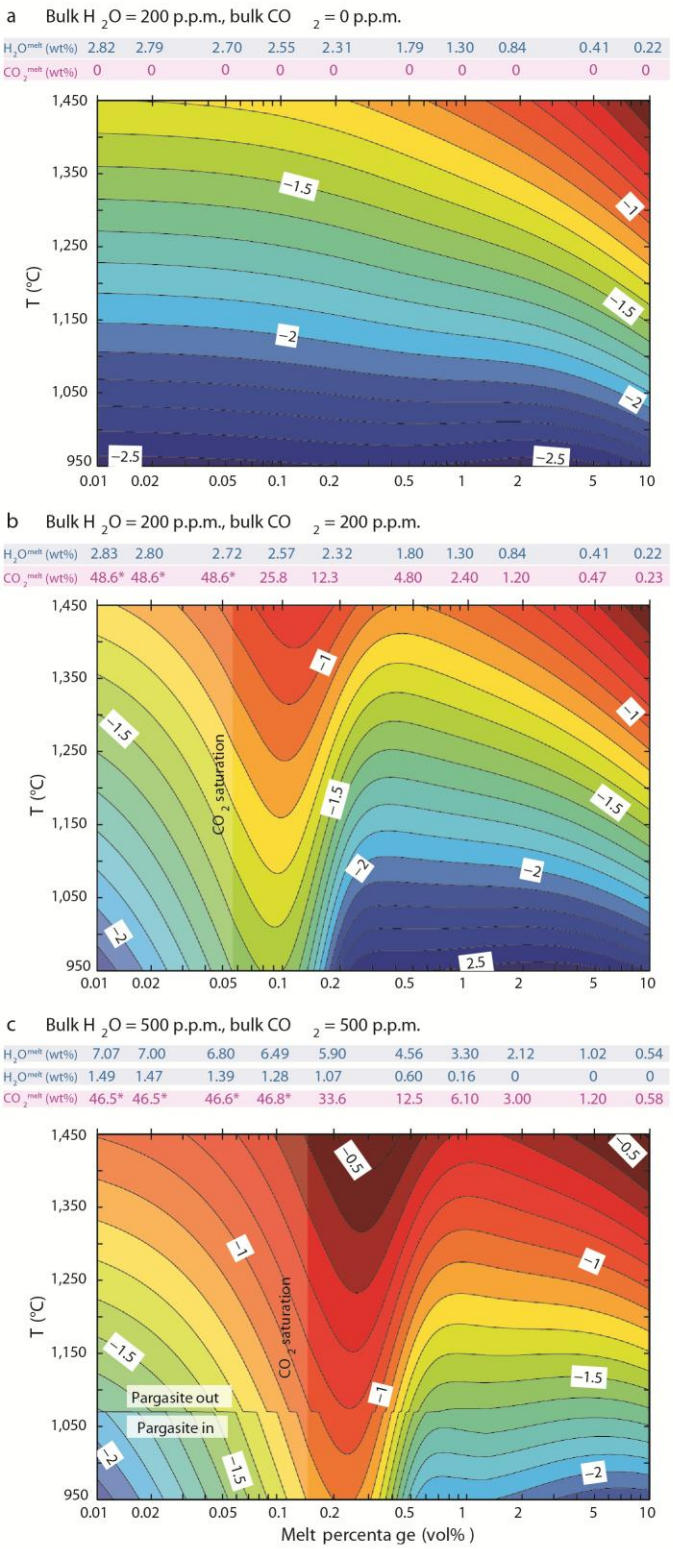

Figure 2. The incipient melt effect on the electrical conductivity of depleted and enriched carbonated peridotites. The conductivity of partially molten peridotite (log values; conductivity increases from cold to warm colours) is reported as a function of melt content and temperature

for (a) CO_2-free peridotite with 200 ppm H_2O and (b, c) depleted and enriched CO_2-bearing hydrous systems. H_2O partitions between minerals and melt, and CO_2 distributes in melt only (Methods). Addition of CO_2 triggers a peak in conductivity at 0.1-0.3 vol.% of melt, where the intergranular liquid is CO_2-rich and therefore highly conductive. At higher degrees of melting, the bulk conductivity decreases since volatiles are diluted in the melt (melt H_2O and CO_2 are tabulated atop each panel), which becomes basaltic. A peridotite with 0.1 vol.% carbonated basalt is as conductive as with 10 vol.% basalt. Two sets of melt H_2O contents are given for the bottom panel (500 ppm H_2O and CO_2), which correspond to pargasite-saturated (low T<1070°C, italics) and paragsite-undersaturated (T>1070°C, normal) melt water contents.

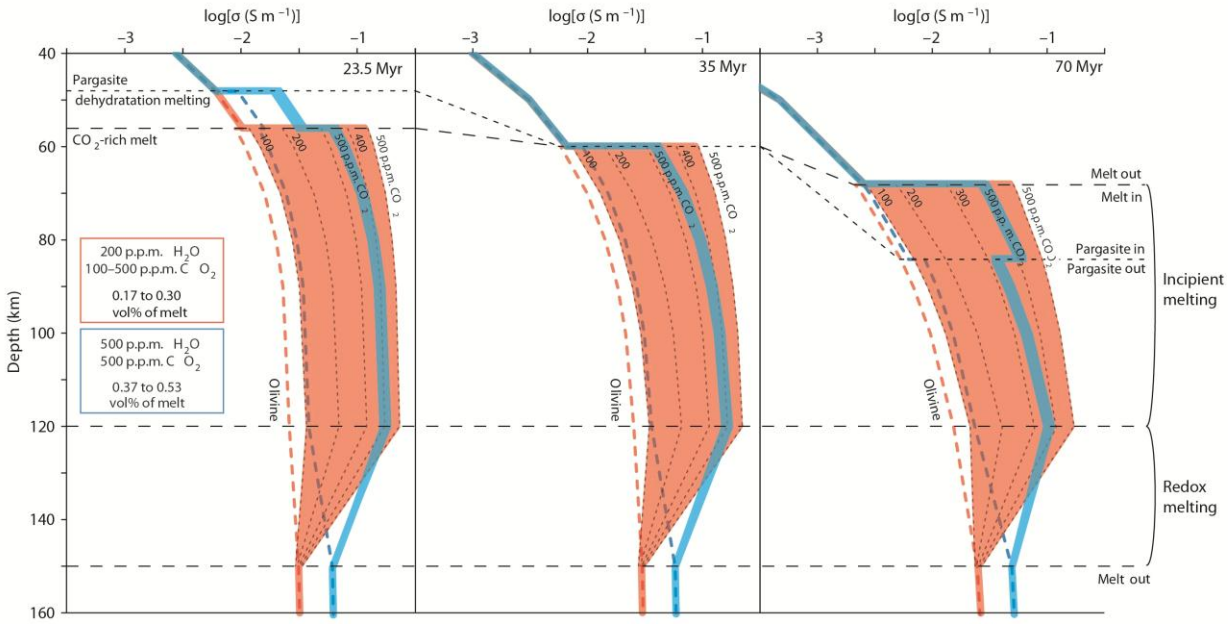

Figure 3. Petrologically-based conductivity profiles across the incipient melting region under the lithosphere-asthenosphere boundary for various ages. Top axis indicates electrical conductivity and how it varies with depth during cooling of the lithosphere for ages of 23.5, 35 and 70 Ma (see choices of geotherm in Fig.4). Conductivities were calculated according to the same model used in Fig. 2 (Methods). Several electrical discontinuities are predicted at variable depths based on the phase-equilibria relationships shown in fig. SI8; the most striking conductivity jumps is related to the upper and lower boundaries of incipient melting (55-150 km). The volatile depleted and enriched mantles are considered and one can appreciate that the conductivity during incipient melting is strongly correlated to CO_2 contents (grey dashed lines labelled from 100 to 500 ppm).

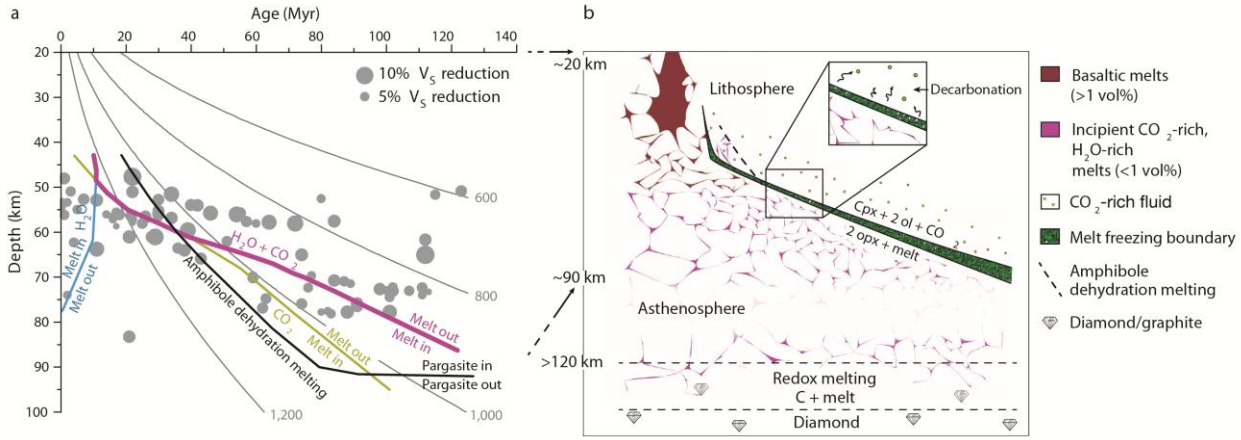

Figure 4. The oceanic seismic low velocity zone bracketed by the upper and lower boundary of incipient melting. (A) Oceanic crustal ages versus depth of seismic discontinuities (Vs reductions) marking the LAB (grey circles[8]) beneath the Pacific Ocean. Colour curves designate the solidi for hydrated (200 ppm H_2O; blue), carbonated (green) and H_2O-undersaturated carbonated (purple) peridotites. Isotherms (grey curves) are calculated from a half-space sudden cooling model, assuming[8] ΔT = 1350°C, an average plate velocity of 8 cm•yr^{-1} and a thermal diffusivity of 1 mm²•s^{-1}. Varying the plate velocity does not change the plot. (B) A visual picture capturing the domain of incipient melting in the oceanic low velocity zone. The LVZ is lower-bounded by the redox melting[22,23] and upper-bounded by the decarbonation[14] leading to the freezing of incipient melts. This boundary constitutes an impermeable layer leaving a clinopyroxene-rich residue and a CO_2-rich vapour phase.

Extended Data Figures

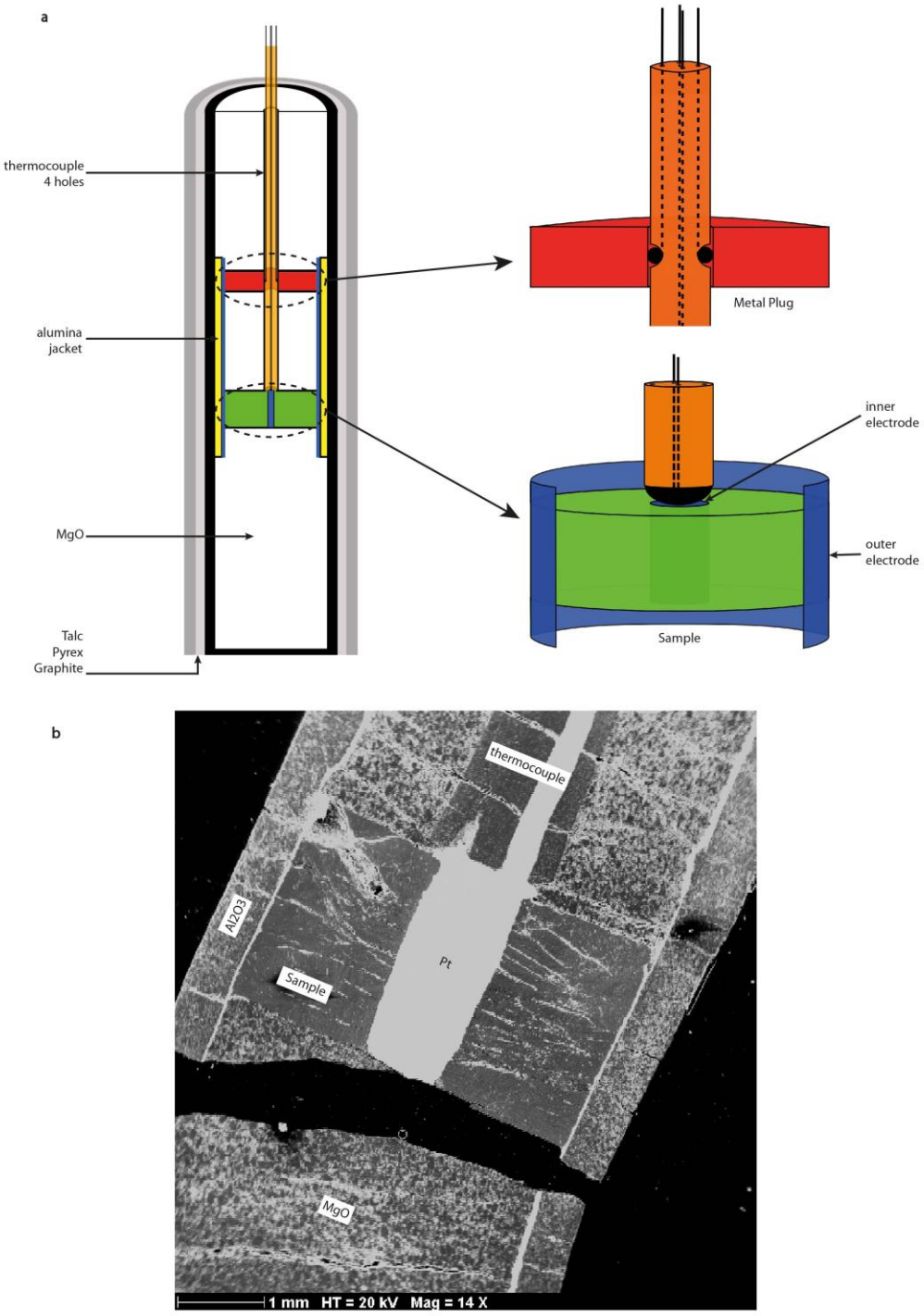

Extended Data Figure 1: Set-up of electrical conductivity measurement using four wires : **a**, Modified piston–cylinder assembly for electrical conductivity measurements using a four-wire configuration. The cored sample (in green) contains in its centre an inner electrode in platinum (in blue). A platinum foil (in blue) surrounds the sample, which extends upwards and downwards from the sample and corresponds

to the outer electrode. The sample is sandwiched by machined MgO ceramics (in white). The electrode-sample assemblage is isolated from the graphite furnace by an Al_2O_3 jacket (in yellow). The four-electrode wires are emplaced using a four-hole Al_2O_3 tube (in orange). Two of these wires, that is, the thermocouple, are in contact with the inner electrode, whereas the outer electrode is in contact with two other wires by means of a top Ni plug (in red). **b**, SEM image of the assemblage of sample C after experiments (up to 1,463 °C and 3 GPa). We observed an average decrease of 20% compared to the initial cell geometry (corresponding to the porosity loss during melting). Cell geometry parameters (h, r_{in} and r_{out} in equation (2)) are determined from SEM images for each sample.

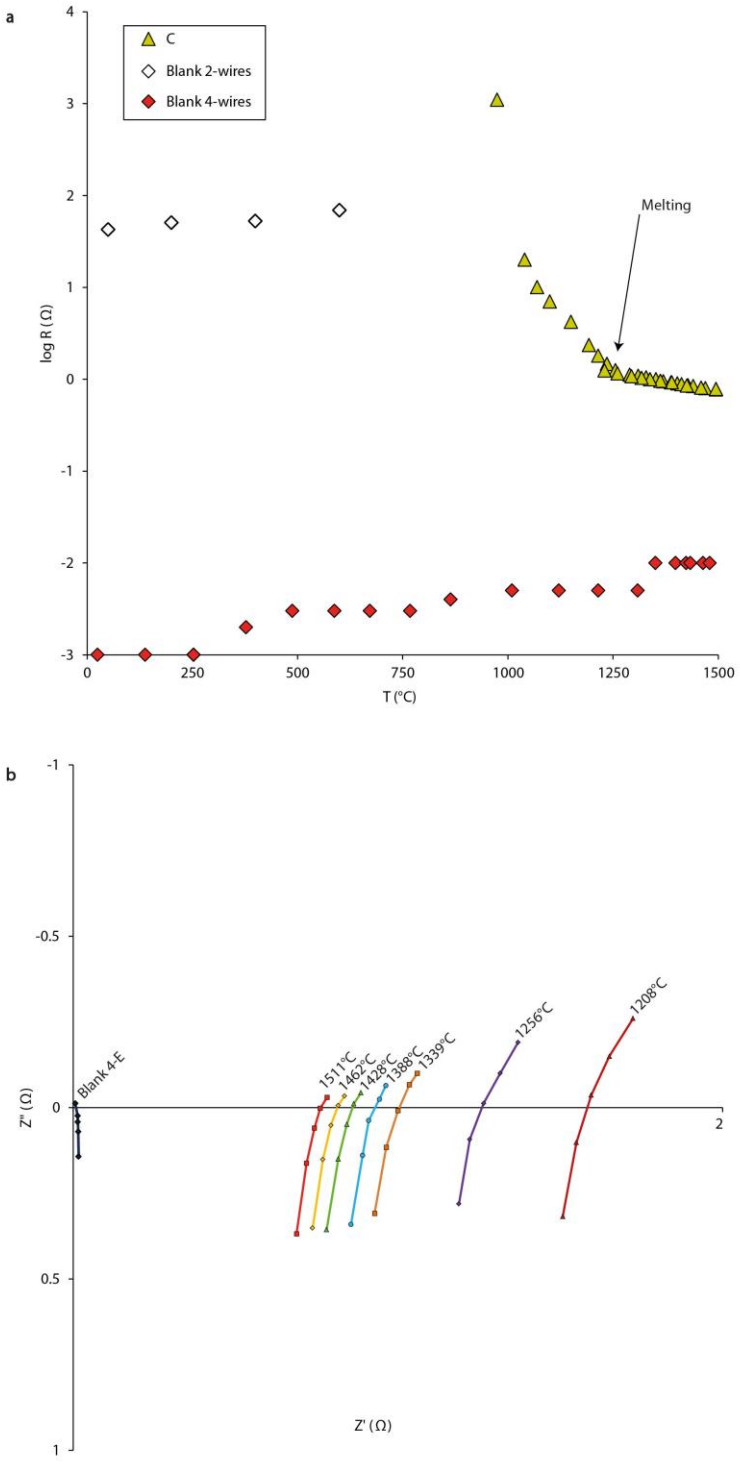

Extended Data Figure 2: Measured resistance of molten carbonate versus nickel : **a**, The electrical cell resistance versus temperature. We show the resistance of a sample made of nickel measured using either a two-wire set-up (empty diamond) or a four-wire set-up (red diamond). There are several orders

of magnitude of difference between the two measurements, showing that the two-wire setup is not suitable at all for conductive materials. We also show the resistance of carbonate in a four-wire set-up (sample C, molten at $T > 1{,}230$ °C; green triangle). **b**, Impedance spectra obtained on molten carbonate (sample C) at 3 GPa as a function of temperature. Impedance spectra show vertical lines, indicating an inductance-dominated signal for all temperatures. The resistance is taken from the intercept with the horizontal axis. Data are obtained at frequencies ranging from 19,905 to 315,479 Hz. The black line represents an impedance spectrum of a nickel sample (blank) obtained with a four-wire configuration at 1,464 °C.

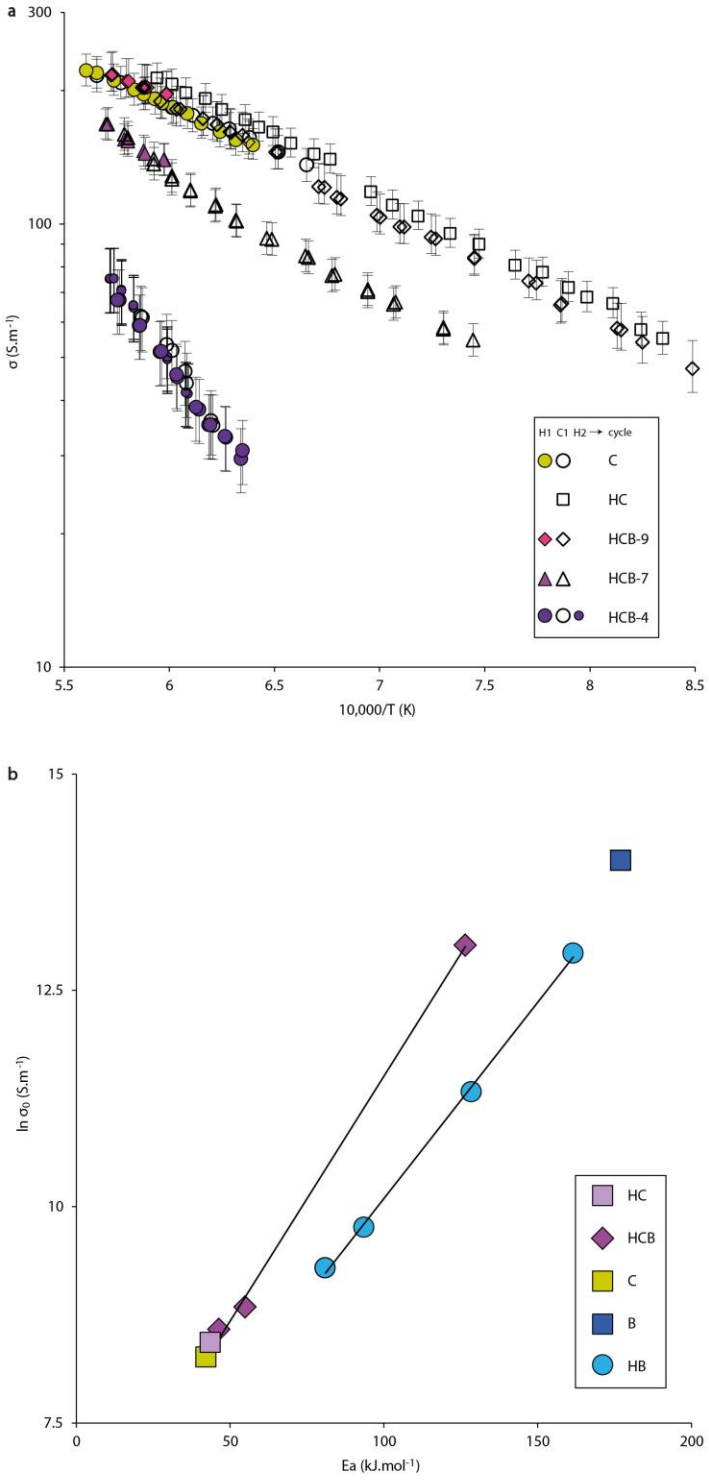

Extended Data Figure 3: Electrical conductivity measurements : **a**, Electrical conductivity versus reciprocal temperature measured on carbonated melts and hydrous carbonated basalts. Samples: a carbonated melt (C), a hydrous carbonated melt (HC), and three hydrous carbonated basalts with H_2O

contents ranging from 4.43 to 9.22 wt% (HCB-9, HCB-7 and HCB-4) and CO_2 contents ranging from 10.39 to 23.32 wt%. To complete Fig. 1, we distinguished heating–cooling temperature cycles and reported error bars. Large solid symbols, heating cycle (H1); open symbols, cooling cycle (C1); small solid symbols, second heating cycle (H2) (compare with Extended Data Table 2a). The error bars include uncertainties in the geometrical factors of the samples and in the measured resistance. **b**, Compensation plots showing the correlation between activation energy, E_a, and pre-exponential terms, $\ln(\sigma_0)$. Hydrous basalts (HB) are from the experimental data set of ref. 7 between 1,200 and 1,500 °C, and the data point for the dry basalt (B) is from ref. 32. The dry carbonated melt (C), the hydrous carbonated melts (HC) and the hydrous carbonated basalts (HCB) are from this study (see Extended Data Table 2b for the Arrhenius parameters).

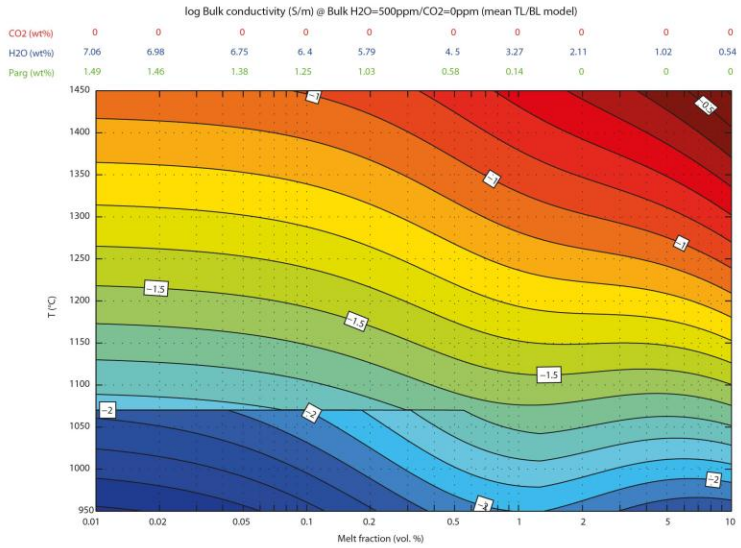

Extended Data Figure 4: The incipient melt effect on the electrical conductivity of an H_2O-enriched, CO_2-free peridotite : This figure completes the scenarios illustrated in Fig. 2. The conductivity of partially molten peridotite, in which H_2O partitions between minerals and melt (Methods), is reported as a function of melt content and temperature for CO_2-free peridotite with 500 p.p.m. H_2O (log values; conductivity increases from cold to warm colours). The discontinuity at T = 1,070 °C is due to pargasite amphibole breakdown (Extended Data Fig. 5) that redistribute H_2O between NAMs and the melt as explained in the Methods. Melt H_2O contents (blue if pargasite out, green if pargasite in) are tabulated above the panel.

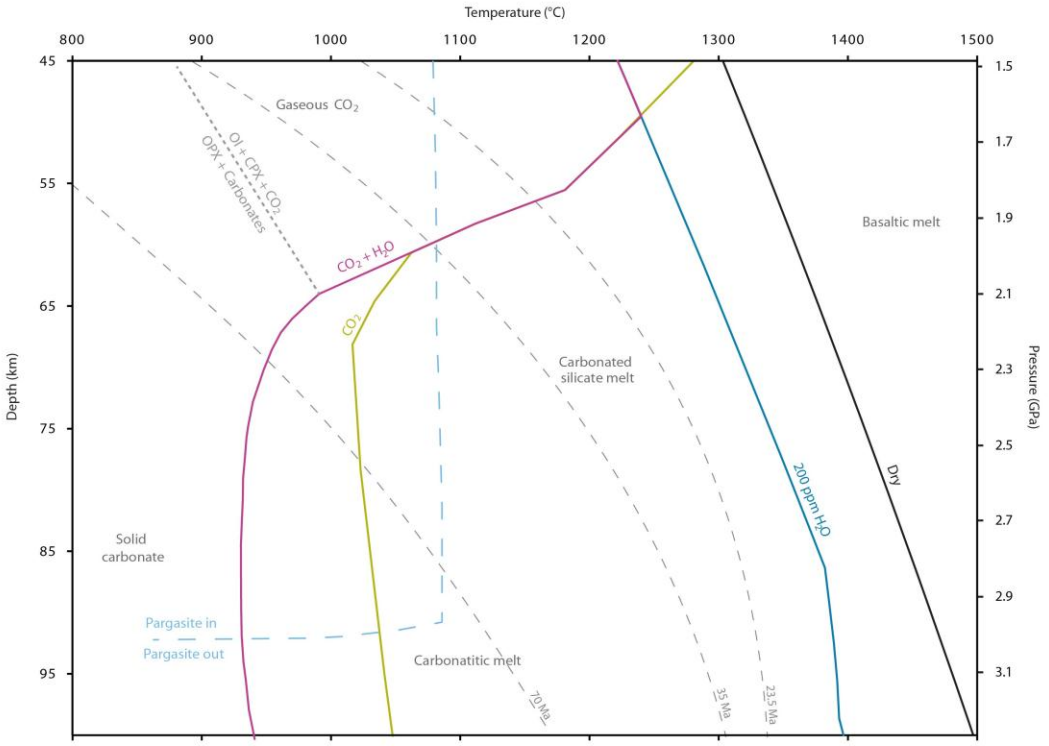

Extended Data Figure 5: Melting curves for different bulk peridotitic systems as functions of temperature and depth : The solidus of dry peridotite (black curve) is calculated from ref. 53. The dehydration solidus of nominally anhydrous peridotite at 200 p.p.m. H_2O (blue curve) is modelled from ref. 9. The dehydration solidus of pargasite lherzolite is based on ref. 10. The nominally anhydrous carbonated, fertile peridotite solidus is based on ref. 54 and references therein (green curve). The H_2O-undersaturated carbonated, fertile peridotite curve (purple curve) corresponds to the solidus of a

pyrolite with 0.5–2.5 wt% CO_2 and 0.3 wt% H_2O (ref. 14). For pressures ≤1.7 GPa, carbonated melts are unstable and gaseous CO_2 prevails. We connected the melting curve of CO_2-bearing peridotite to that of the dry peridotite at low pressures, which slightly differs from previously published phase diagrams. We considered that, for $P \leq 1.7$ GPa, gaseous CO_2 must have a negligible influence on the peridotite solidus due to the small solubility of CO_2 in basaltic melts[55]. Similarly, at low pressures, the H_2O-undersaturated carbonated, fertile peridotite solidus was connected to the dehydration solidus of nominally anhydrous peridotite (considering peridotite with 200 p.p.m. H_2O), neglecting the presence of pargasite owing to the NAM's H_2O capacity storage.

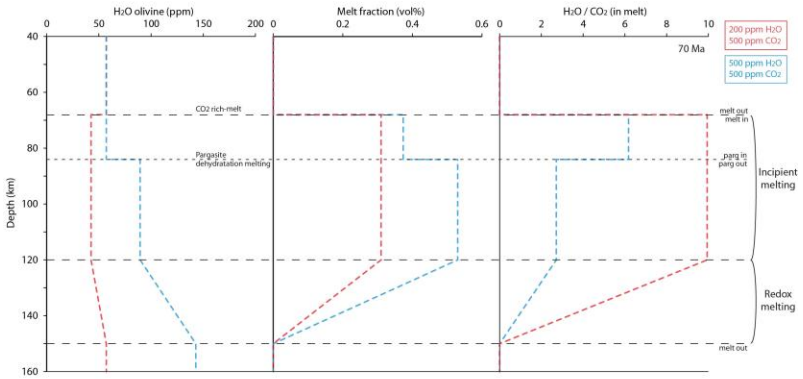

Extended Data Figure 6: Phase equilibria control on H_2O–CO_2 partitioning, ultimately resulting in a change in conductivity as shown in Fig. 3 : We show changes in H_2O content in olivine (left), melt fraction (centre) and melt CO_2/H_2O (right) for the 70-Myr age used for calculation in Fig. 3. We use two illustrative compositions: bulk with 200 p.p.m. H_2O and 500 p.p.m. CO_2 and bulk with 500 p.p.m. H_2O and 500 p.p.m. CO_2.

Extended Data Table 1: Chemical composition of samples before and after electrical conductivity measurements

a

	Carbonated Melt			Hydrous Carbonated Basalt			Starting Material	
	dry		hydrous					
Sample	C	C +	H C	H C B -9	H C B -7	H C B -4	Dolomite	Basalt
SiO_2	0.24	0.24	0.02	5.23	15.67	31.32	0.27	52.18
TiO_2	0.03	0.03	0.02	0.20	0.56	1.10	0.03	1.81
Al_2O_3	0.02	0.02	0.01	1.52	4.54	9.07	0.02	15.11
FeO	0.20	0.20	0.02	0.82	2.41	4.80	0.22	7.99
MgO	18.68	18.68	23.79	22.16	18.90	14.01	20.76	7.49
CaO	26.50	26.50	32.19	30.01	25.66	19.13	29.44	10.42
Na_2O	0.02	5.87	0.01	0.31	0.91	1.82	0.02	3.02
K_2O	0.03	0.03	0.01	0.07	0.21	0.41	0.03	0.67
MnO	0.03	0.03	0.01	0.03	0.06	0.11	0.03	0.17
P_2O_5	0.33	0.33	0.33	0.36	0.38	0.41	0.37	0.49
NaCl	10.00	-	7.50	6.75	5.25	3.00	-	-
Total	56.07	51.92	63.91	67.46	74.55	85.18	51.19	0.00
CO_2	43.93	48.08	25.91	23.32	18.15	10.39	48.81	0.05
H_2O	-	-	10.18	9.22	7.30	4.43	-	0.60

b

	Carbonated Melt			Hydrous Carbonated Basalt		
	dry		hydrous			
Sample	C	C +	H C	H C B -9	H C B -7	H C B -4
SiO_2	0.4	0.32	0.26	5.49	15.83	32.12
TiO_2	0.03	0.03	0.01	0.29	0.22	1.05
Al_2O_3	0.07	0.02	0.35	1.25	4.82	10.43
FeO	0.01	0.03	0.03	0.04	0.29	3.98
MgO	17.76	18.02	23.39	22.94	20.69	14.52
CaO	26.63	26.74	32.05	30.29	26.16	19.25
Na_2O	5.32	5.65	3.75	3.95	3.54	3.02
K_2O	0.05	0.03	0.01	0.1	0.05	0.48
MnO	0.04	0.03	0.05	0.08	0.03	0.1
P_2O_5	0.33	0.33	0.04	0.38	0.27	0.51
NaCl	6.12	-	4.51	4.02	3.11	1.92
Total	56.76	51.19	64.45	68.83	75.01	87.38
CO_2	-	-	10.11	8.09	6.89	3.46
H_2O	43.24	48.81	25.44	23.08	18.10	9.16

Extended Data Table 2: Temperature range of electrical conductivity measurements and adjusted Arrhenius parameters

a

	C	C+	HC	HBC-9	HBC-7	HBC-4
Heating cycle	0-1511	0-1404	-	1397-1472	1383-1482	1304-1465
Cooling cycle	1511-1120	-	1410-650	1472-850	1482-1070	1465-1338
Heating cycle 2	-	-	-	-	-	1338-1470

b

	Ea ($J.mol^{-1}$)	error ($J.mol^{-1}$)	ln σ_0 ($S.m^{-1}$)	error ($S.m^{-1}$)
C	42150	700	8.26	0.05
C+	41950	1330	8.2	0.12
HC	43460	670	8.47	0.05
HBC-9	46360	2300	8.58	0.17
HBC-7	54900	3400	8.84	0.32
HBC-4	126500	2700	13.02	0.2

Extended Data Table 3: Parameters used for equations (3) and (4)

	H_2O	CO_2
a	88,774	789,166
b	0.3880	0.1808
c	73,029	32,820
d	4.54E-05	5.50E-05
e	5.5607	5.7956